

# Using open data to benchmark internal dynamics of phosphatidylcholine in molecular dynamics simulations

Hanne S. Antila,<sup>†</sup> Tiago Ferreira,<sup>‡</sup> Matti Javanainen,<sup>¶</sup> O. H. Samuli Ollila,<sup>§</sup> and Markus S. Miettinen<sup>\*,†</sup>

<sup>†</sup>*Department of Theory and Bio-Systems, Max Planck Institute of Colloids and Interfaces, 14424 Potsdam, Germany*

<sup>‡</sup>*NMR Group — Institute for Physics, Martin-Luther University Halle-Wittenberg, 06120 Halle (Saale), Germany*

<sup>¶</sup>*Add Matti to author list?*

<sup>§</sup>*Institute of Biotechnology, University of Helsinki, 00014 Helsinki, Finland*

E-mail: markus.miettinen@mpikg.mpg.de

## Abstract

Molecular dynamics (MD) simulations are a widely used tool to study the atomistic structure and dynamics of biomembranes. It remains unknown, however, how well the conformational dynamics observed in MD simulations correspond to those occurring in real life phospholipids. The accuracy of such time scales in MD can be assessed by comparing against the effective correlation times of the C-H bonds measured in nuclear magnetic resonance experiments (J. Chem. Phys. 142 044905 (2015)).

Here, we analysed the conformational dynamics of phospholipids as produced by several commonly used MD models (force fields). None of the tested force fields reproduced all the effective correlation times within experimental error, much like they do not provide accurate conformational ensemble (J. Phys. Chem. B 119 15075 (2015)). However, the dynamics observed in CHARMM36 and Slipids were more realistic than those seen in the Amber Lipid14, OPLS-based MacRog, and GROMOS-based Berger force fields, which were all characterized by unrealistically slow dynamics in the glycerol backbone.

## 1 Introduction

Ever since the conception of the Protein Data Bank (PDB) and the NCBI GenBank, the access to open data has shaped the state of the art of research in life sciences. Not only has the development of new characterisation techniques (such as molecular replacement<sup>1</sup> in macromolecular x-ray crystallography and 3D electron microscopy) been aided by the existence of these databases,<sup>2</sup> but perhaps more importantly they have lead to entirely new ways of doing science in the form of bio- and chem-informatics, enabling data-driven discovery of drugs,<sup>3</sup> materials<sup>4</sup> as well as identifying<sup>5,6</sup> and filling<sup>7</sup> gaps in the databanks themselves. All in all, open access to standardised and searchable pools of experimental data, constantly extending owing to a collaborative effort, has enabled scientific progress that is well beyond the resources of one single research group.

Much of the development of the PDB and other biomolecular databanks into the core resources they are today has been fueled by the push from scientific journals and funders towards public availability and conservation of data. In addition to experimental results, these

principles have more recently extended to simulation trajectories of biomolecules, leading to databases of dynamic information. Inspired by the success of bio- and cheminformatics, we seek to exploit this and demonstrate, for the first time, the viability of creating new scientific knowledge analysis of pre-existing, open access simulation data.

More specifically, we will analyze a wide set of publicly available phosphatidylcholine (PC) phospholipid bilayer molecular dynamics (MD) simulation trajectories, produced by using different MD models (force fields). In addition of simulations of one component bilayers under standard conditions, we study trajectories under varying hydration, salt concentration, and cholesterol content. We test whether different force fields reproduce the experimentally observed internal dynamics of PC lipids, and investigate if the dynamics extracted from various models share common features that can be used to draw general conclusions on the system, to suggest future directions for experimental research, and to avoid potential pitfalls in future simulations of bilayers.

Our choice for the system of interest is inspired by the importance of phospholipids not only as the building blocks of cell membranes but also as emerging candidates for micro- and nanotechnology, such as the use of liposomes as microcapsules in targeted drug delivery.<sup>8</sup> These molecules consist of a hydrophilic phosphate head group, which is connected to two hydrophobic fatty acid tails via a glycerol backbone. The ability of lipids to self assemble into bilayer membrane (and other) configurations is a direct consequence of this dual nature. Although biological membranes are complex mixtures of multiple lipid types as well as other molecules, lamellar phospholipid bilayers with one or few lipid types serve as an important model system, that have been successfully used to decipher, *eg.*, possible molecular mechanisms behind anesthetics,<sup>9?</sup> the effect of cholesterol on membrane structure,<sup>10?</sup> and the functioning of membrane proteins<sup>11</sup> **1.add more references.** In particular, MD simulations of these model systems have been widely used<sup>9,10,12? -15</sup> to provide an atomistic view on the biomembranes,

and hold vast potential in making further connections between their structure and function.

The significance for investigating the conformational dynamics of lipids in bilayer simulations is two-fold. Firstly, when exploring static properties of the bilayers, it is crucial to assess how well the simulations have converged. In order to extract reliable statistics, the conformations sampled have to represent the equilibrium distribution with enough transitions between states. Indeed, simulations of a single (1,2-dioleoyl-sn-glycero-3-phosphocholine) DOPC lipid using the CHARMM32b2 force field indicated that the conformations sampled do not replicate the equilibrium distribution even after 500 ns;<sup>16</sup> also, the C-H bond dynamics of the Berger model was shown<sup>14</sup> to be too slow at the glycerol region of 1-palmitoyl-2-oleoylphosphatidylcholine (POPC) compared to correlation times extracted from NMR experiments.

Secondly, for complete picture of membrane functioning, knowledge on the bilayer dynamics in addition to equilibrium measurements are needed. The ability of the MD model to reproduce the relative abundance of different dynamical processes is crucial for the correct interpretation of pathways leading to, *e.g.*, membrane deformation<sup>17</sup> and lipid-induced conformational<sup>18,19</sup> changes of membrane proteins. The availability of such model could also greatly guide both the configuration and interpretation of NMR experiments used to extract dynamical information from lipid assemblies. **2.the following paragraph could be merged into methods, opinions?** Our analysis of the lipid dynamics is based on two quantities, the spin-lattice relaxation rate  $R_1$  and the effective correlation time  $\tau_e$ , both experimentally available through NMR measurements, and directly calculable from all-atom MD simulations. Out of the two, the  $R_1$  rates (or the corresponding  $T_1$  times) have been traditionally used to assess both the conformational dynamics of lipids in experimental bilayers<sup>20-24</sup> and the dynamics produced by lipid MD models in bilayer simulations.<sup>20,22,23,25</sup> However, relying on  $R_1$  only has several drawbacks **3.do all flavors (31P,13C,...) have the same**

**problem?** It builds on an underlying rotation-diffusion model, its sensitivity is typically limited to C–H bond reorientation with time scales  $\sim 1$ -10 ns, and measurements at several temperatures and magnetic field strengths are required to fully characterize the dynamics. To address these deficiencies, two of us introduced a procedure<sup>14</sup> for quantifying the effective C–H correlation times ( $\tau_e$ )—a model free quantity that encompasses conformational dynamics with time scales up to hundreds of nanoseconds—from bilayer systems. Most importantly, increasing  $\tau_e$  always signals some type of slowdown in the C–H bond dynamics, making the interpretation less ambiguous than for  $R_1$ , where slowdown in the dynamics can lead to either an increase or a decrease of  $R_1$  value.<sup>14</sup>

In summary, this work provides first comprehensive comparison of dynamics of different phosphatidylcholine MD models, where both pure bilayers and the model response to changing conditions and composition is explored. The study is conducted using data-driven exploration of pre-existing, publicly available simulation trajectories to demonstrate the power of open, well documented data in creating new knowledge at a lowered computational cost and high potential for automation.

## 2 Methods

## 3 Theoretical Background

<sup>13</sup>C NMR experiments investigating lipid conformational dynamics take advantage of the fact that the relaxation of <sup>13</sup>C magnetization dominantly happens via the dipolar coupling of the carbon with the magnetic moments of the protons bound to it, with the symmetry axis of the interaction aligning with the C–H bond. The spectral density depicting the <sup>13</sup>C relaxation rates (at frequency  $\omega$ ) is expressed as

$$j(\omega) = 2 \int_0^\infty \cos(\omega\tau) g(\tau) d\tau, \quad (1)$$

which is the Fourier transformation of the C–H bond second order autocorrelation function at

time  $\tau$

$$g(\tau) = \langle P_2(\vec{\mu}(t) \cdot \vec{\mu}(t + \tau)) \rangle, \quad (2)$$

where  $\vec{\mu}(t)$  is the unit vector in the direction of the C–H bond at time  $t$  and  $P_2$  is the second order Legendre polynomial. The angular brackets depict averaging over time. The autocorrelation function can be expressed as the product of two functions

$$g(\tau) = g_f(\tau) g_s(\tau), \quad (3)$$

where  $g_f(\tau)$  characterizes fast decays owing to, for example, the molecular rotations, and  $g_s(\tau)$  describes slow decays that originate from, e.g., the lipid diffusion. The two components, along with the oscillation due to magic angle spinning at the  $\sim$ kHz region, are depicted in Fig. 1. Correlation time of 4.2 ms has been estimated for multilamellar POPC samples at 300 K for the slow modes, whereas in liquid crystalline lipid bilayers the faster  $g_f(\tau)$  decays to a plateau value  $S_{CH}^2$  within a few hundred nanoseconds.<sup>14</sup> The C–H bond order parameters

$$S_{CH} = \frac{1}{2} \langle 3 \cos^2 \theta - 1 \rangle, \quad (4)$$

where  $\theta$  is the angle between the bond and the bilayer normal, are measured in NMR experiments from this plateau. As  $S_{CH}$  describes the conformational ensemble of the molecule, the fast-decaying component of the rotational correlation function intuitively depicts the time needed to sample these conformations. The characteristic time can be quantified via the effective correlation time

$$\tau_e = \int_0^\infty \frac{g_f(\tau) - S_{CH}^2}{1 - S_{CH}^2} d\tau. \quad (5)$$

The integrand can be viewed as a reduced and normalized correlation function

$$g'_f(\tau) = \frac{g_f(\tau) - S_{CH}^2}{1 - S_{CH}^2}. \quad (6)$$

That is,  $\tau_e$  is defined as the area under  $g'_f(\tau)$ , as graphically depicted in Fig. 1b. **4.Maybe also add 1C that explicitly shows  $g'_f$ ?** It is easily seen that in

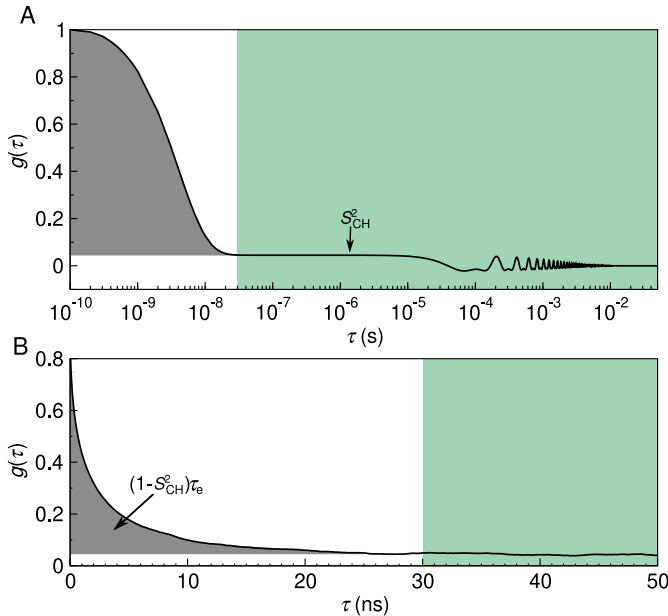


Figure 1: The autocorrelation function  $g(\tau)$  a) The fast mode (white background) and the slow mode (shaded green) of the correlation function along with the oscillation owing to magic angle spinning. The fast mode decays to a plateau quantifying the  $S_{CH}$  while the slow mode gives the final descent to zero. b) Illustration of typical C–H bond autocorrelation function obtained from a MD simulation. The gray area under the curve gives a means of quantifying the  $\tau_e$ .

the presence of more long-lived correlations  $\tau_e$  grows, signaling that more time is needed for full conformational sampling.

The spin-lattice relaxation rate  $R_1$  defines the time-scale on which  $^{13}\text{C}$  longitudinal magnetization equilibrates. It is defined as

$$R_1 = \frac{d_{CH}^2 N_H}{20} [j(\omega_H - \omega_C) + 3j(\omega_C) + 6j(\omega_H + \omega_C)], \quad (7)$$

where  $N_H$  is the number of bound hydrogens,  $\omega_H$  and  $\omega_C$  are the Larmor frequencies for  $^1\text{H}$  and  $^{13}\text{C}$ , and  $d_{CH}$  is the rigid dipolar coupling constant. For the methylene bond,  $d_{CH}/2\pi$  approximately equals to -22 kHz.

The dependency of  $R_1$  on the spectral densities  $j$  at the Larmor frequencies means that the  $R_1$  value depicts the relative amounts of relaxation processes with time-scales near the

inverses of the Larmor frequencies. Since the Larmor frequencies depend on the field strength used in the NMR measurements, this typically makes  $R_1$  sensitive to  $\sim 1$ – $10$  ns time-scales. Importantly, a change in  $R_1$  thus indicates a difference in the relative amounts of processes within the detection window, and therefore does not give information on the modulation of the total sampling rate.

### 3.1 Experimental data acquisition and analysis

All the experimental quantities were collected from the literature **5.Except are they, or mostly from Tiago and re-analysed from raw data?** sources referred at the respective figures **6.How to refer to experimental data from Tiago?**.

### 3.2 Simulational data acquisition and analysis

The simulation trajectories used in this work were collected from the Zenodo repository ([zenodo.org](https://zenodo.org)) with majority of the data originating from the NMRlipids Project<sup>13,26</sup> ([nmrlipids.blogspot.fi](https://nmrlipids.blogspot.fi)). Table 1 lists, with references to the trajectory files, the simulations of pure POPC bilayers at/near room temperature and at full hydration. Table 2 lists simulations including cholesterol; Table 3 simulations with varying hydration; and Table 4 at increasing NaCl concentration. Additional computational details of each of the simulations are available at the cited Zenodo entry.

The simulational data were analysed using in-house scripts. These are available on GitHub<sup>?</sup> along with a Python notebook outlining an example analysis run. After downloading the necessary files from Zenodo, the trajectory was processed with Gromacs `gmx trjconv` to make the molecules whole. The C–H bond order parameters  $S_{CH}$ , see Eq. (4), were then calculated with the `calcOrderParameters.py`<sup>?</sup> script that uses the MDanalysis<sup>?</sup> Python library. The C–H bond correlation functions  $g(\tau)$ , see Eq. (2), were calculated with Gromacs5.1.4<sup>?</sup> `gmx rotacf`; note that on simula-

**Table 1: Analyzed simulations of POPC lipid bilayers at standard conditions.**

force field	$N_l^a$	$N_w^b$	$T^c(K)$	$t_{\text{anal}}^d(\text{ns})$	files <sup>e</sup>
Berger-POPC-07 <sup>27</sup>	128	7290	298	50	[28]
CHARMM36 <sup>29</sup>	128	5120	303	140	[30]
	34	1020	300	140	[31]
MacRog <sup>32</sup>	128	6400	310	200	[33]
Lipid14 <sup>34</sup>	72	2234	303	50	[35]
Slipids <sup>36</sup>	200	9000	310	500	[37]
ECC <sup>38</sup>	128	6400	300	300	[39]

<sup>a</sup>Number of POPC molecules.

<sup>b</sup>Number of water molecules.

<sup>c</sup>Simulation temperature.

<sup>d</sup>Trajectory length used for analysis.

<sup>e</sup>Reference for the openly available simulation files.

**Table 2: Analyzed simulations of cholesterol-containing POPC bilayers.**

force field POPC/cholesterol	$c_{\text{chol}}^a$	$N_{\text{chol}}^b$	$N_l^c$	$N_w^d$	$T^e(K)$	$t_{\text{anal}}^f(\text{ns})$	files <sup>g</sup>
Berger-POPC-07 <sup>27</sup>	0%	0	128	7290	298	50	[28]
/Höitje-CHOL-13 <sup>10,40</sup>	50%	64	64	10314	298	60	[41]
CHARMM36 <sup>29</sup>	0%	0	128	5120	303	140	[30]
	50%	80	80	4496	303	200	[43]
MacRog <sup>32</sup>	0%	0	128	6400	310	200	[33]
	50%	64	64	6400	310	200	[33]
Slipids <sup>36</sup>	0%	0	200	9000	310	500	[37]
	50%	200	200	18000	310	500	[37]

<sup>a</sup>Bilayer cholesterol content (mol %).

<sup>b</sup>Number of cholesterol molecules.

<sup>c</sup>Number of POPC molecules.

<sup>d</sup>Number of water molecules.

<sup>e</sup>Simulation temperature.

<sup>f</sup>Trajectory length used for analysis.

<sup>g</sup>Reference for the openly available simulation files.

tional (fast) time scales  $g = g_s g_f = g_f$ . To obtain the  $g'_f$ , the  $S_{\text{CH}}$  were used to normalize the  $g_f$  following Eq. (6).

The effective correlation times  $\tau_e$  were then calculated by integrating  $g'_f(\tau)$ , see Eqs. (5) and (6), over time from  $\tau = 0$  until  $\tau = t_0$ . Here  $t_0 = \min\{t | g'_f(t) = 0\}$ , that is,  $t_0$  is the first time point at which  $g'_f$  reached zero. If  $g'_f$  did not reach zero within  $t_{\text{anal}}/2$ , the  $\tau_e$  was not determined, but we report only its upper and lower error estimates.

To estimate the error on  $\tau_e$ , we first estimate the error on  $g'_f(\tau)$ . There are two sources of error,  $g_f(\tau)$  and  $S_{\text{CH}}^2$ . Performing linear error

**Table 3: Analyzed simulations of lipid bilayers under varying hydration level.**

force field	lipid	$n_{w/l}^a$	$N_l^b$	$N_w^c$	$T^d(K)$	$t_{\text{anal}}^e(\text{ns})$	files <sup>f</sup>
Berger-POPC-07 <sup>27</sup>	POPC	57	128	7290	298	50	[28]
Berger-DLPC-13 <sup>45</sup>	DLPC <sup>g</sup>	24	72	1728	300	80	[46]
	DLPC <sup>g</sup>	16	72	1152	300	80	[47]
	DLPC <sup>g</sup>	12	72	864	300	80	[48]
Berger-POPC-07 <sup>27</sup>	POPC	7	128	896	298	60	[49]
Berger-DLPC-13 <sup>45</sup>	DLPC <sup>g</sup>	4	72	288	300	80	[50]
CHARMM36 <sup>29</sup>	POPC	40	128	5120	303	140	[30]
	POPC	15	72	1080	303	20	[51]
	POPC	7	72	504	303	20	[52]
MacRog <sup>32</sup>	POPC	50	288	14400	310	40	[53]
	POPC	15	288	4320	310	100	[53]
	POPC	10	288	2880	310	100	[53]

<sup>a</sup>Water/lipid molar ratio.

<sup>b</sup>Number of lipid molecules.

<sup>c</sup>Number of water molecules.

<sup>d</sup>Simulation temperature.

<sup>e</sup>Trajectory length used for analysis.

<sup>f</sup>Reference for the openly available simulation files.

<sup>g</sup>1,2-didodecanoyl-sn-glycero-3-phosphocholine.

**7. The data points here do not match those in Fig. 5B.**

**MacRog in Fig. 5B: 50, 25, 10, 5 w/l, and C36 in**

**Fig. 5B: 40, 31, 15, 7 w/l.**

**8. The  $t_{\text{anal}}$  for MacRog here do not match Ref. 53**

**(100 ns  $\rightarrow$  50 ns)?**

**Table 4: Analyzed simulations of POPC lipid bilayers at varying NaCl concentration.**

force field POPC/ions	[NaCl] <sup>a</sup> (mM)	$N_{\text{Na}}^b$	$N_l^c$	$N_w^d$	$T^e(K)$	$t_{\text{anal}}^f(\text{ns})$	files <sup>g</sup>
CHARMM36 <sup>29</sup>	0	0	128	5120	303	140	[30]
	346	13	72	2085	303	80	[55]
	692	26	72	2085	303	73	[56]
	947	37	72	2168	303	60	[57]
MacRog <sup>32</sup>	0	0	128	6400	310	400	[33]
	103	27	288	14554	310	90	[59]
	207	54	288	14500	310	90	[59]
	311	81	288	14446	310	80	[59]
	416	108	288	14392	310	90	[59]
Slipids <sup>36</sup>	0	0	200	9000	310	500	[37]
	130	21	200	9000	310	100	[61]
	999	162	200	9000	310	200	[62]

<sup>a</sup>NaCl concentration, calculated as  $[\text{NaCl}] = N_{\text{Na}} \times [\text{water}] / N_w$ , where  $[\text{water}] = 55.5 \text{ M}$ .

<sup>b</sup>Number of  $\text{Na}^+$  ions, equal to number of  $\text{Cl}^-$  ions.

<sup>c</sup>Number of POPC molecules.

<sup>d</sup>Number of water molecules.

<sup>e</sup>Simulation temperature.

<sup>f</sup>Trajectory length used for analysis.

<sup>g</sup>Reference for the openly available simulation files.



propagation on Eq. (6) gives

$$\Delta g'_f(\tau) = \left| \frac{1}{1 - S_{\text{CH}}^2} \right| \Delta g_f(\tau) + \left| \frac{2(g_f(\tau) - 1) S_{\text{CH}}}{(1 - S_{\text{CH}}^2)^2} \right| \Delta S_{\text{CH}}. \quad (8)$$

Here the  $\Delta S_{\text{CH}}$  was determined as in the NMR-lipids Project: the standard error of the mean of the  $S_{\text{CH}}$  of all the  $N_l$  individual lipids.<sup>13</sup> Similarly, we determined the error on  $g_f(\tau)$  by first determining an individual correlation function  $g_f^m(\tau)$  for each lipid  $m$  over the whole trajectory, and then obtaining the error estimate  $\Delta g_f(\tau)$  as the standard error of the mean over the  $N_l$  lipids. Importantly, this gives an error estimate at each time point  $\tau$ .

To obtain the lower error estimate on  $\tau_e$ , we integrate the function  $g'_f(\tau) - \Delta g'_f(\tau)$  over time from  $\tau = 0$  until  $\tau = t_l$ . Here

$$t_l = \min \left\{ \left\{ t \mid g'_f(t) - \Delta g'_f(t) = 0 \right\}, \frac{t_{\text{anal}}}{2} \right\}. \quad (9)$$

That is,  $t_l$  is the first time point at which the lower error estimate of  $g'_f$  reached zero; or  $t_l = t_{\text{anal}}/2$ , if zero was not reached by that point.

To obtain the upper error estimate on  $\tau_e$ , we first integrate the function  $g'_f(\tau) + \Delta g'_f(\tau)$  over time from  $\tau = 0$  until  $t_u = \min \{t_0, t_{\text{anal}}/2\}$ . Note, however, that this is not yet sufficient, because there could be slow processes that our simulation was not able to see. Although these would contribute to  $\tau_e$  with a low weight, their contribution over long times could still add up to a sizable effect on  $\tau_e$ . That said, it seems feasible to assume (see Fig. 1A) that there are no longer-time contributions to  $g_f$  than something that decays with a time constant of  $10^{-6}$  s. We use this as our worst case estimate to assess the upper error on  $\tau_e$ , and assume that all the decay from the time point  $t_u = \min \{t_0, t_{\text{anal}}/2\}$  onwards comes solely from this slowest process. The additional contribution to the upper error for  $\tau_e$  then reads  $\Delta g'_f(t_u) \times (\exp(-t_u/10^{-6} \text{ s}) - \exp(-1)) \times 10^{-6} \text{ s}$ .

#### 9. Discuss the possibility of skewed error distributions?

The  $R_1$  rates were calculated using Eq. (7),

with the spectral density  $j(\omega)$  obtained for a given normalized correlation function  $g'_f$  by fitting it with a sum of  $N = 71$  exponentials

$$g'_f(\tau) \approx \sum_{i=1}^N \alpha_i e^{-\tau/\tau_i}, \quad (10)$$

with logarithmically spaced time-scales  $\tau_i$  ranging from 0.1 ps to 1  $\mu\text{s}$ , and then calculating the spectral density of this fit based on the Fourier transformation<sup>14</sup>

$$j(\omega) = 2(1 - S_{\text{CH}}) \sum_{i=1}^N \alpha_i \frac{\tau_i}{1 + \omega^2 \tau_i^2}. \quad (11)$$

The  $R_1$  rate of a given C-H bond was first calculated separately for each lipid  $m$  (using Eq. (7) with  $N_H = 1$ , and  $j^m(\omega)$  obtained for the normalized correlation function  $g_f^m$ ). The thus obtained  $N_l$  measurements per bond were then assumed independent: Their mean gave the  $R_1$  rate of the bond, and standard error of the mean its uncertainty. The total  $R_1$  rate of a given carbon was obtained as a sum of the  $R_1$  rates of its C-H bonds. When several carbons were known to have contributed to the experimental  $R_1$  rate of a carbon segment, the carbon-wise  $R_1$  rates were averaged to obtain the segment-wise  $R_1$  rate. The segment-wise error estimates were obtained by standard error propagation, starting from the uncertainties of the  $R_1$  rates of the C-H bonds.

To gain some qualitative insight on the time scales at which the main contributions to the (headgroup)  $R_1$  rates arise, we also looked at 'cumulative'  $R_1$  rates,  $R_1(\tau)$ . These contained just those contributions in the sum of Eq. (11) for which  $\tau_i < \tau$ . Note that here the  $g'_f$  averaged over lipids was used; therefore, the 'cumulative'  $R_1(\tau \rightarrow \infty)$  does not necessarily have exactly the same numerical value as the actual  $R_1$ .

Finally, we note that the fit of Eq. (10) provides an alternative to estimating  $\tau_e$ , because

$$\tau_e = \int_0^\infty g'_f(\tau) d\tau \approx \sum_{i=1}^N \alpha_i \tau_i. \quad (12)$$

When the simulation trajectory is not long enough for the correlation function to reach the

plateau, integrating  $g'_f$  gives a lower bound estimate for  $\tau_e$ , while the sum of Eq. (12) includes also (some) contribution from the longer-time components via the fitting process. However, in practice the fit is often highly unreliable in terms of depicting the long tails of the correlation function, and thus in this work we chose to quantify  $\tau_e$  using the area under  $g'_f$ , and estimate its errors as discussed in detail above.

## 4 Results and Discussion

In the following, we discuss phospholipid internal dynamics in six different MD force fields, first at standard conditions (pure POPC bilayers, full hydration, no salt; see Table 1 for simulation details and Fig 2 for results). We then proceed to cover a wider range of experimentally, biologically, and computationally relevant conditions, and investigate how the dynamics change when cholesterol is added to the bilayer (Table 2 and Fig. 4), when hydration level is reduced (Table 3 and Fig. 5), and when monovalent salt is added to the solution (Table 4 and Fig. 7).

One should keep in mind that none of the force fields we study produces all the C–H bond order parameters,  $S_{CH}$ , within experimental accuracy.<sup>13</sup> In other words, the structural ensembles simulated do not exactly match the structural ensemble occurring in reality, that is, these simulations are not a true computational microscope. Consequently, the  $\tau_e$  times and  $R_1$  rates depict the dynamics of sampling a somewhat different phase space for each model. To this end, we will try to avoid overly detailed discussion on the models and rather concentrate on detecting common and qualitative trends.

### Effective correlation times $\tau_e$ at standard conditions.

The left panels of Fig. 2 compare the  $\tau_e$  obtained for fully hydrated POPC bilayers in experiments (black) and in the six different MD force fields (color).

Qualitatively, every force field captures the general shape of the  $\tau_e$  profile: Dynamics slows

down towards the glycerol backbone in both the headgroup and in the tails. Quantitatively, MD has a tendency towards slightly too fast dynamics in the membrane core, but at the water-facing interface MD is typically clearly too slow. CHARMM36 and Slipids show the best overall performance—although the  $\tau_e$  in Slipids exhibit a qualitatively wrong, decreasing, trend from  $g_3$  to  $g_1$ .

The slowness of MD around the glycerol backbone is consistent with previous results for the Berger model.<sup>14</sup> It also agrees with the insufficient conformational sampling of glycerol backbone torsions observed in 500-ns-long CHARMMc32b2<sup>63,64</sup> simulations of a DOPC lipid.<sup>16</sup>

It is worth noting that although temperature varied across these openly available simulation data, it was in no case lower than in the experiment. As decreasing the temperature would increase the  $\tau_e$ —as indicated by the CHARMM36 simulations at different temperatures—any overestimation of  $\tau_e$  by MD would get worse, were the simulations done at the experimental 298 K.

### $R_1$ rates at standard conditions.

The panels on the right side of Fig. 2 compare experimental and simulated  $R_1$  rates under the same conditions as for the  $\tau_e$  on the left.

The  $R_1$  comparison distinctly differs from what is seen for  $\tau_e$ . Some models that do very well for  $\tau_e$ , do rather poorly for  $R_1$ , such as CHARMM36 in the  $\gamma$ ,  $\beta$ , and  $\alpha$  segments. Also examples to the contrary are seen: MacRog gives particularly fitting  $R_1$  rates for the  $\beta$ ,  $\alpha$ ,  $g_3$ , and  $g_1$  segments, although it systematically overestimates their  $\tau_e$ .

To appreciate the implications of such differences, let us recall that matching our experimental  $R_1$  rates (measured at 125 MHz) is a necessary condition for a given force field to have correct rotational dynamics at the  $(2\pi \times 125 \text{ MHz})^{-1} \approx 1 \text{ ns}$  time scale. In contrast,  $\tau_e$  reflects all the sub- $\mu\text{s}$  time scales (Fig. 1).

Figure 2 reveals a few cases where both  $R_1$  and  $\tau_e$  (almost) match experiments, suggesting (almost) correct rotational dynamics at all relevant time scales. For example, Slipids

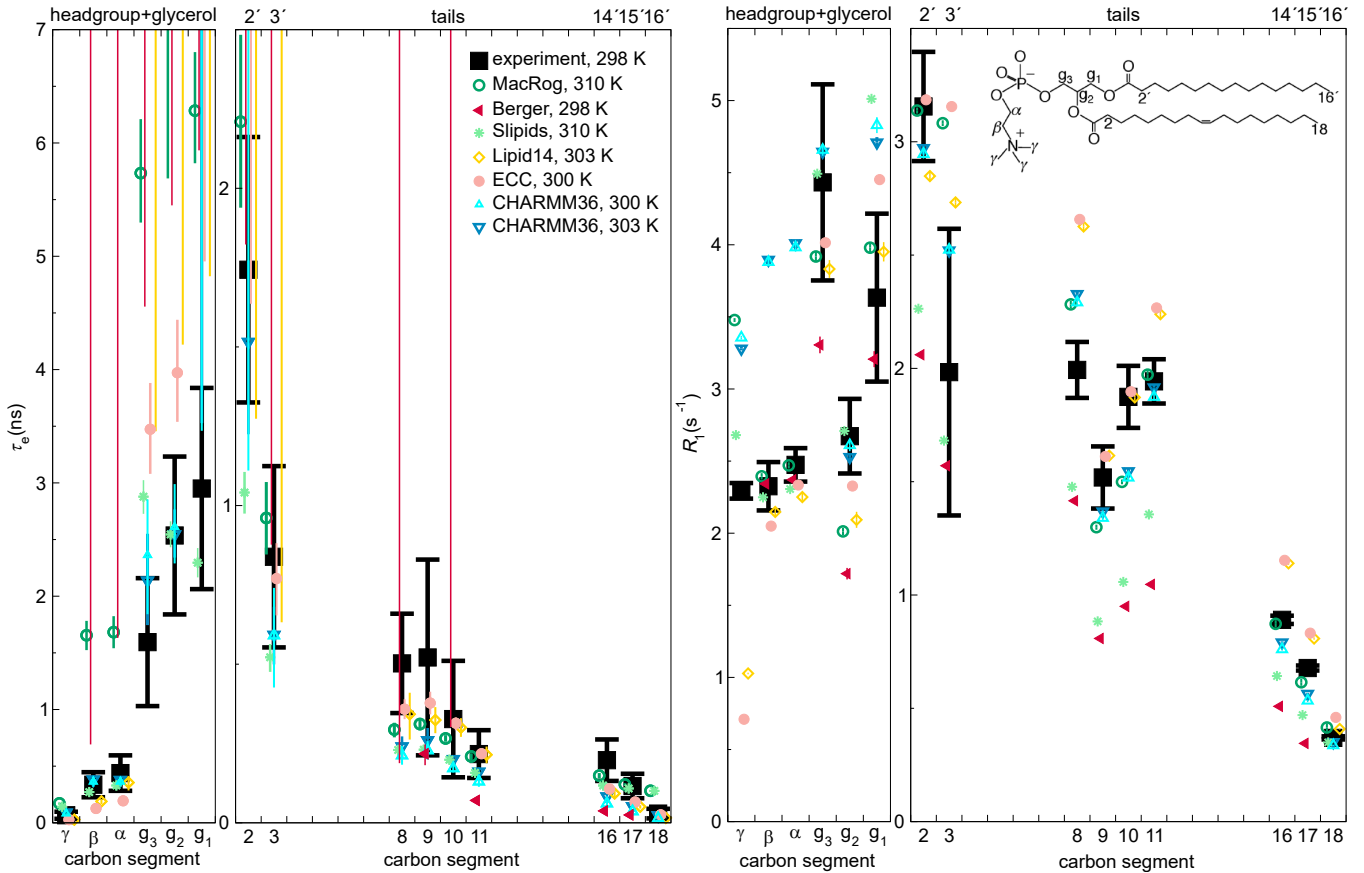


Figure 2: Effective correlation times ( $\tau_e$ , left panels) and  $R_1$  rates (right panels) in experiments (black) and MD simulations (colored) of POPC bilayers in  $L_\alpha$  phase under full hydration. Inset on the right shows the POPC structure and carbon segment labelling. Each plotted value contains contributions from all the hydrogens within its carbon segment; the data for segments 8–11 are only from the sn-2 (oleoyl) chain, whereas the (experimentally non-resolved) contributions of both tails are included for segments 2–3 (2'–3' in the sn-1 chain) and 16–18 (14'–16'). Simulation data are only shown for the segments for which there exists experimental data. For  $\tau_e$ , a simulation data point indicates the average over hydrogens; however, if  $\tau_e$  could not be determined for all hydrogens, only the error bar (extending from the mean of the lower to the mean of the upper error estimates) is shown. The methyl segments ( $\gamma$ , C18, and C16') in Berger are left out, because for a united atom model the hydrogens must be constructed post-simulation from the heavy atom locations, and the protonation algorithm does not preserve the methyl C–H bond dynamics. Table 1 provides further simulation details. Error bars for the experimental values reflect error estimate of XXX.

10. Experimental error estimate changed since the data were originally published; needs to be explained to the reader.

11. How to refer to the experiments? Not really from previous publication because of re-analysis.

does a good job for the  $\beta$  and  $\alpha$  segments; CHARMM36 for the  $g_3$ ,  $g_2$ , C2 and C3; Lipid14 and ECC for the oleoyl double bond; and MacRog for the tail end segments. (Notably, all force fields are qualitatively correct in giving that  $g_2$  has the smallest  $R_1$  of the glycerol segments and segment 9 of the oleoyl double bond segments. That said, no MD model captures that the  $R_1$  rates for the oleoyl segments

8, 10, and 11 are all roughly equal.)

In Fig. 2 there are also cases where a matching  $R_1$  is accompanied by a larger-than-experimental  $\tau_e$ . Such a combination suggests that MD does well at the 1 ns scale, but has too slow long-time dynamics. The most prominent example of this is MacRog for  $\beta$ ,  $\alpha$ , and the glycerol region.

Figure 2 also has cases where  $\tau_e$  matches ex-



periments, but  $R_1$  does not. This indicates a cancelation of errors for the  $\tau_e$ : The wrong dynamics at the 1 ns scale are compensated by wrong dynamics at other time scales. This is seen to be the case in all five all-atom force fields for the  $\gamma$  segment, and for CHARMM36 in  $\beta$  and  $\alpha$ . As CHARMM36 on the whole did rather well for both  $R_1$  and  $\tau_e$ , let us next study this shortcoming on the headgroup  $R_1$  rates in some more detail.

## Dynamics of headgroup segments in CHARMM36.

Figure 3A zooms in on the headgroup ( $\gamma$ ,  $\beta$ ,  $\alpha$ ) segments, whose  $\tau_e$  were not clearly visible on the scale of Fig. 2. For all three segments, CHARMM36 matches the experimental  $\tau_e$ , but overestimates  $R_1$ . No other force field does any better for  $\gamma$ , but for the  $\beta$  and  $\alpha$  segments Slipids provides almost perfect dynamics.

The time scales that most contribute to  $R_1$  rates are highlighted by the 'cumulative'  $R_1(\tau)$  (Fig. 3B). It is obtained, as detailed in Methods, by including in the sum of Eq. (11) only terms with  $\tau_i < \tau$ . Consequently, at  $\tau \rightarrow \infty$  the 'cumulative'  $R_1(\tau)$  approaches the actual  $R_1$ .

Figure 3B shows that for models that overestimate the  $R_1$  rate of  $\gamma$  (MacRog, CHARMM36, and Slipids, see Fig. 3A) the major contribution to  $R_1$  arises at  $\tau > 50$  ps. In contrast, for those that underestimate the  $R_1$  rate (Lipid14 and ECC, see Fig. 2) the major contribution arises at  $\tau < 50$  ps. This also manifests in the distribution of fitting weights ( $\alpha_i$  in Eq. (10)) in Fig. 3C: The earlier the non-zero weights occur, the smaller is the resulting  $R_1$ .

For the  $\beta$  and  $\alpha$  segments, Fig. 3B shows that the main contribution to  $R_1$  rates arises between 200 ps and 2 ns. As CHARMM36 has the largest weights of all models in this window (Fig. 3C), it overestimates  $R_1$ . Slipids, which has simultaneously  $R_1$  and  $\tau_e$  correct, has its largest weights at  $\tau < 200$  ps. Indeed, considerable weights at short time scales ( $< 10$  ps in  $\alpha$  for Lipid14, ECC, Berger) and at long time scales ( $> 10$  ns in both  $\beta$  and  $\alpha$  for MacRog and Berger) do not manifest at all in the  $R_1$  rates. However, the latter contribute heavily

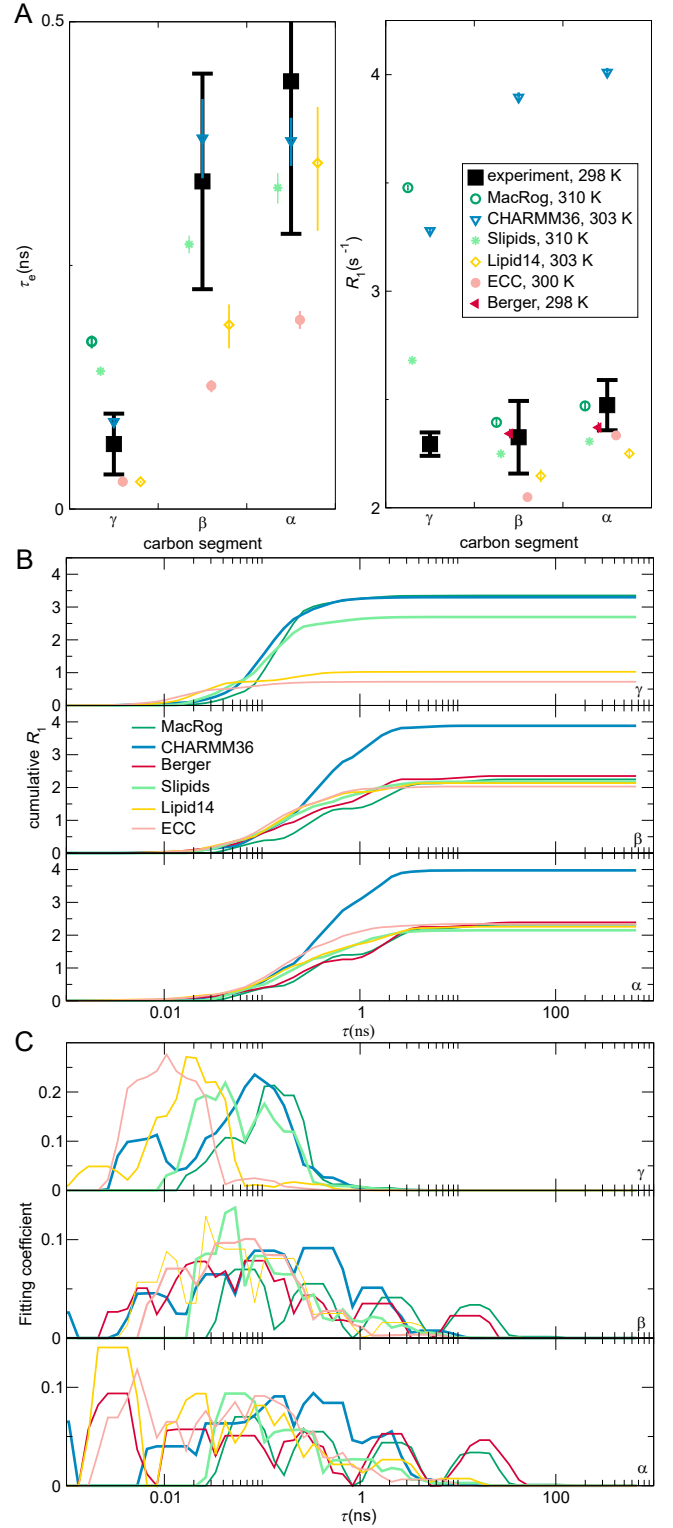


Figure 3: (A) Zoom on the headgroup  $\tau_e$  (left panel) and  $R_1$  (right). (B) 'Cumulative'  $R_1$  (see Methods for definition) of the  $\gamma$  (top panel),  $\beta$  (middle), and  $\alpha$  (bottom) segments. (C) Prefactor weights  $\alpha_i$  from Eq. (10) of  $\gamma$  (top),  $\beta$  (middle), and  $\alpha$  (bottom). In B and C, a sliding average over 5 neighboring data points is shown.

on  $\tau_e$ , which is thus considerably overestimated by MacRog and Berger (Fig. 2).

What are the motions in the 0.2–2 ns window that are over-presented in CHARMM36? Identifying them and speeding them up would improve the model dynamics. However, the connection between the fitted correlation times and the correlation times of distinct motional processes such as dihedral rotations and lipid wobbling turns out to be highly non-trivial; we thus refrain from further analysis here.

## Effect of cholesterol.

The experimental effective correlation times  $\tau_e$  (Fig. 4A, top panels) show that when cholesterol is added, the glycerol region conformational dynamics slow down markedly. The tail segments slow down too, the effect increasing towards the backbone. In stark contrast, however, the  $\tau_e$  of headgroup segments ( $\gamma$ ,  $\beta$ ,  $\alpha$ ) appear fully unaffected by cholesterol. Furthermore, cholesterol induces no measurable change in the headgroup  $\beta$  and  $\alpha$  segment dynamics at short ( $\sim 1$  ns) time scales, as demonstrated by the experimental  $R_1$  rates (Fig. 4A, lower panels). That said, there is a measurable change to  $R_1$  at  $\gamma$ , at the oleoyl double bond, and at the tail end.

All the force fields investigated qualitatively reproduce slow downs of  $\tau_e$  (see Fig. 4B): Slipids gives the best magnitude estimates, while CHARMM36 and MacRog clearly overestimate the changes at the glycerol, C2, and C3 carbons. Notably, MacRog (and Berger?) predicts an erroneous slow down also for the  $\beta$  and  $\alpha$  carbons, for which experiments detect no change. Also, while CHARMM36 correctly shows no change in  $\tau_e$  of the  $\gamma$ ,  $\beta$ , and  $\alpha$  carbons, it does predict a clearly non-zero  $\Delta R_1$  for all three, indicative of some inaccuracies in the headgroup rotational dynamics. Such inaccuracies might affect the recent findings<sup>65</sup> obtained using CHARMM36 that (at least at small cholesterol concentrations) the headgroups of PCs neighbouring a cholesterol (within 6.6 Å) spend more time on top of the cholesterol than elsewhere; such arrested rotations should manifest on  $\tau_e$  and  $R_1$ . Interest-

ingly, the tail  $\Delta R_1$  seem to be pretty well captured by all three all-atom force fields, whereas Berger fails to capture the change at the oleoyl bond.

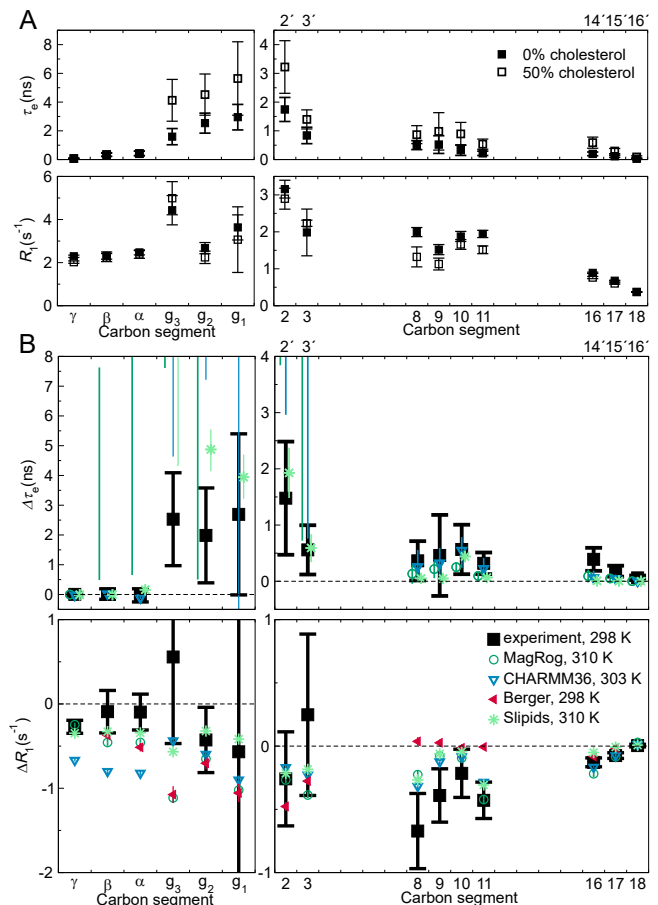


Figure 4: Effect of bilayer cholesterol content. (A) The experimental effective correlation times  $\tau_e$  (top panels) and  $R_1$  rates (bottom) in a pure POPC bilayer and in a bilayer containing 50% cholesterol. The data were measured at 298 K and full(?) hydration. (B) The change in  $\tau_e$  ( $\Delta\tau_e$ , top panels) and  $R_1$  ( $\Delta R_1$ , bottom), both in experiments and in MD simulations, when bilayer composition changes from pure POPC to 50% cholesterol. Berger not shown for  $\Delta\tau_e$ , because the open data available were insufficient to determine meaningful error estimates. Error estimates for the simulated  $\Delta\tau_e$  are the maximal possible based on the errors at 0% and 50% cholesterol; for other data regular error propagation is used. Table 2 provides further simulation details; for segment labeling, see Fig. 2.

**12.@Hanne: Double check that the calculation of errors in (B) was as the caption describes.**

## Effect of drying.

Figure 5A shows how a mild dehydration affects C-H bond dynamics in the PC headgroup and glycerol backbone; the plot compares the experimental effective correlation times  $\tau_e$  measured for POPC at full hydration and for DMPC (1,2-dimyristoyl-sn-glycero-3-phosphocholine) at 13 waters per lipid. The  $\tau_e$  are the same within experimental accuracy. This is in line with what was seen experimentally when adding cholesterol (Fig. 4): The headgroup ( $\gamma$ ,  $\beta$ ,  $\alpha$ )  $\tau_e$  are unaffected by structural differences (such as the presence of cholesterol or the tail types) in the glycerol and tail regions. In addition, Fig. 5A indicates that a mild dehydration does not alter the  $\tau_e$  in the headgroup and glycerol regions.

Figure 5B shows the effects of dehydration in three MD models. Combination of the unrealistically slow dynamics especially in the glycerol backbone (Fig. 2) and the relatively short lengths of the openly available trajectories (Table 3) led to large uncertainty estimates. However, in the  $\gamma$  segment there is clearly no effect above 13 w/l in CHARMM36 and MacRog, in agreement with the experiments; lower water contents show a slow down, especially in MacRog below 10 w/l. Similarly, the  $\beta$  and  $\alpha$  segments show no detectable change above 13 w/l for CHARMM36 and Berger, in agreement with the experiments; below 10 w/l Berger shows a slowdown, and in CHARMM36 the slowdown manifests as an abrupt increase of the uncertainty estimate. For the glycerol segments, due to the large uncertainties, only qualitative trends of the lower error estimate can be looked at: For CHARMM36 the lower error estimate stays almost constant all the way until 7 w/l, for Berger and MacRog it suggests a slowdown starting already from  $\sim 20$  w/l.

These simulational findings indicate that experiments at hydration levels below 10 w/l would also show an increase in  $\tau_e$ . This prediction is in line with the exponential slowdown of the headgroup conformational dynamics upon dehydration that was indicated by  $^2\text{H}$ -NMR  $R_1$  measurements of DOPC bilayers:  $R_1 \sim \exp(-n_{w/l}/4)$ .<sup>67</sup> The slowdown was attributed to the reduction in the effective volume

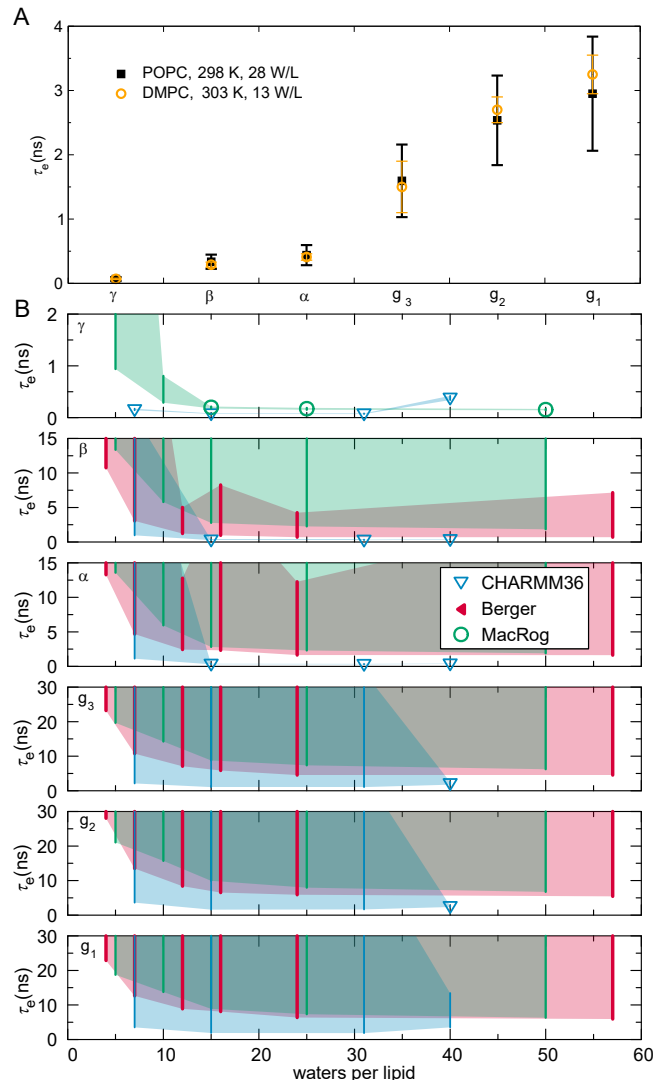


Figure 5: Effect of drying on effective correlation times in headgroup and glycerol backbone. (A) Experimental  $\tau_e$  for DMPC (from Ref. 66) at low hydration do not significantly differ from the  $\tau_e$  for POPC at full hydration. (B) Calculated  $\tau_e$  for POPC at decreasing hydration in three MD models. Note that three Berger data points are from DLPC bilayers (dashed). Points give the mean of segment hydrogens, if  $\tau_e$  could be determined for all hydrogens; else only the error bar (extending from the mean of the lower to the mean of the upper uncertainty estimates) is shown; the area delimited by the error bars is shaded for visualization. See Table 3 for simulation details.

**13. How to refer to full hydration POPC data?**

**14. Add also the black and orange (i.e. experimental) data points to B.**

available for the headgroup<sup>67</sup> owing to its tilt towards the membrane upon dehydration; the tilt is observed via changes of the lipid headgroup order parameters,<sup>68</sup> and is qualitatively reproduced by all the simulation models.<sup>13</sup>

Figure 6 shows a collection of experimental  $^{13}\text{C}$ -NMR  $R_1$  rates measured at 125 MHz for the headgroup segments at different water contents; in addition to the full hydration POPC data from Fig. 2, DMPC at 13 w/l,<sup>66</sup> and POPC at 20 and 5 w/l<sup>69</sup> are shown. An increasing trend with decreasing hydration is observed for all the segments, indicating changes of headgroup dynamics at short ( $\sim 1$  ns) time scales. Interestingly, only CHARMM36 captures this, whereas Berger and MacRog present the opposite, decreasing, trend for the  $\beta$  and  $\alpha$  segments.

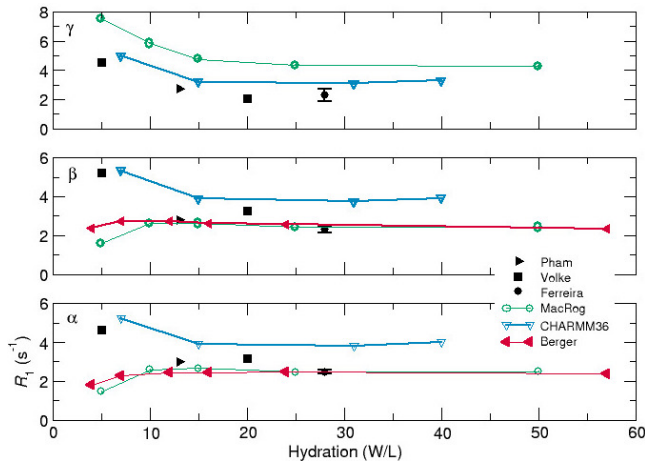


Figure 6: Effect of drying on  $^{13}\text{C}$ -NMR  $R_1$  rates of the headgroup segments (at 125 MHz) in experiments and simulations.

The here discussed slow down should be of significance not only when simulating a bilayer (stack) under low hydration, but also for studies of intermembrane interactions, such as membrane fusion, because these naturally lead to dehydrated conditions when the lipid assemblies approach. Slower dynamics imply that longer simulation times are needed for equilibration, for reliably quantifying the properties of the bilayers, and for observing rare events.

## Effect of salinity.

Finally, we study the response of the MD model dynamics to increasing amounts of monovalent

salt. Experimentally, the modulation of  $\alpha$  and  $\beta$  carbon order parameters upon increasing ion concentration have been used to quantify ion binding to lipid bilayers (the molecular electrometer<sup>26,70</sup>). The order parameters are constant for POPC bilayers under NaCl addition in experiments, indicating negligible ion binding. Based on this, we anticipate the effective correlation times also to be unaffected by monovalent salt, however, to our knowledge no experimental measurements have been conducted to quantify this.

The molecular electrometer has been used to show that most molecular dynamics force fields overestimate the binding of monovalent ions to PC bilayers:<sup>26</sup> In the simulations the modulation of the  $\alpha$  and  $\beta$  carbon order parameters by increasing NaCl concentration was overestimated compared to the experiments, and accompanied by accumulation of ions at the bilayer surface. In Fig. 7 we compare three force fields, one that is known to exhibit pronounced overbinding<sup>26</sup> (MacRog) and two producing more realistic binding affinity (Slipids and CHARMM36). The lateral distribution of  $\text{Na}^+$  ions near the bilayer is quantified in Fig. 7a whereas Fig. 7b shows the change in  $\tau_e$  for increasing salt concentration. Ion accumulation results in a slow down in the effective correlation time that is somewhat proportional to the strength of ion binding. Correlation times extracted from the CHARMM36 model vary only a little (low ion binding) when ion concentration is increased, whereas a slightly more pronounced change is observed with Slipids, and MacRog exhibits a clear slow-down (significant ion binding). This indicates that, similarly to the order parameters,  $\tau_e$  may be useful in investigating the ion binding affinity of lipid bilayers and experimental work exploring this avenue would be interesting.

**15.validity of statement regarding Slipids**

## 5 Conclusions

Q: How is the effective correlation time  $\tau_e$  related to the autocorrelation of the order param-



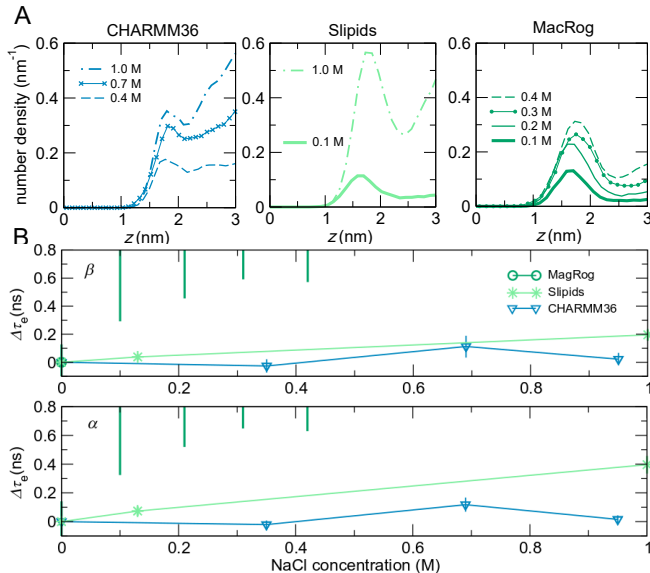


Figure 7: The impact of increasing ionic strength on effective correlation times. a) The density distribution (average over both leaflets) of Na<sup>+</sup> ions as function of distance  $z$  from the bilayer center. The plots for each force field are presented from left to right in the order of increasing ion accumulation. b) Effective correlation times for  $\alpha$  and  $\beta$  C-H bonds in growing NaCl concentration from CHARMM36, Slipids, MacRog POPC simulations. Details on the simulation data are provided in Table 4.

eter  $S_{CH}$ ? After all,  $\tau_e$  does measure the reorientation of the C-H bond, which is clearly related to how fast the  $S_{CH}$  is sampled.

A: In a lipid bilayer, the second order rotational correlation function approaches  $S_{CH}^2$ . The speed of this approach tells how fast the C-H bond orientations are sampled. In the relaxation experiment this speed is measured.

In the C-H bond order parameter experiment one measures how much of the second order rotational correlation is left after all the available C-H bond orientations in the bilayer have been sampled.

That is,  $\tau_e$  does indeed measure how fast the  $S_{CH}^2$  is sampled.

If the relaxation is single-exponential,  $\tau_e$  is the relaxation time of this exponential process. If the relaxation is multi-exponential,  $\tau_e$  is the weighted mean of the corresponding set of relaxation times.

In the multi-exponential case it is a bit hard

to say just based on  $\tau_e$ , how long one needs to sample the  $S_{CH}$ , because this depends also on the above-mentioned weights of the processes.

The main advantage of  $\tau_e$  is that the larger (smaller) it is, the slower (faster) the process is. The same is not true for  $R_1$  or other spin relaxation parameters, because their connection to the molecular dynamics is complicated, and goes through the spectral density, see Eq. (7).

Here, we have investigated the dynamics of phosphatidylcholine molecular dynamics models using publicly available MD trajectories. The MD models are able to qualitatively capture the correlation time profile of POPC—the slow glycerol backbone and the faster dynamics of the headgroup and tail regions—but most are prone to too slow dynamics of the glycerol C-H bonds. In general, these force fields reproduce the experimentally detected  $R_1$  values adequately, indicating that processes at time scales  $\sim 1$  ns are represented but problems arise at longer time-scales. While none of the force fields is able to reproduce all the experimental values, the CHARMM36 POPC model performs well when compared to the effective correlation times, while the Slipids and Lipid14 force field provide realistic  $R_1$  in the PC headgroup and glycerol regions. However, since none of the current MD models reproduce the experimental order parameters, these timescales depict a sampling of a conformational space that does not fully represent the underlying reality.

In addition to the bilayers under standard conditions, we also explored how the dynamics react to the addition of cholesterol, salt, and to the reduction of hydration level. When cholesterol is mixed into the POPC bilayer, the conformational dynamics of the tails and the glycerol regions slows down. Again, the MD models are able to qualitatively capture this, but some also predict an increase in the correlation times for the headgroup carbons, possibly leading to erroneous conclusions. In increasing salt concentration a behaviour reminiscent of the molecular electrometer was observed: Amount of ion binding to the bilayer correlated with the magnitude of slowdown in the correlation times. This could open up the possibility of

using effective correlation times in quantifying the ion binding to lipid bilayers. When reducing the water content, the MD models exhibited somewhat constant correlation times down to  $\sim 15$  waters per lipid in agreement with experimental data. After this, a slow down was observed.**16.hydratation needs some kind of statement of significance.**

By gathering a set of experimental information on the phosphatidylcholine dynamics and underlining some of the typical features of the MD models, this study sets a foundation and a potential roadmap for further improvement of the current force fields. While work is still needed in capturing even the correct order parameters, the dynamics is equally essential part of developing MD into a true computational microscope; after all, it is possible to obtain the correct order parameters just by freezing the system into a set of selected conformations.**17.not very smoothly put, help!**

Finally, this work demonstrates the power of open data in creating new knowledge out of existing trajectories at a reduced computational and labor cost. Although no new simulations were performed for the purpose of this work, we were able to conduct a comprehensive study on the dynamics of MD models under several conditions. An interesting extension would be exploring other lipid headgroups individually as well as performing a comparison of MD model dynamics between headgroup types, as the available simulation data goes well beyond simulations of lipids with the phosphocholine headgroup. If the data are well indexed and documented, this process could be easily automated and has the potential to facilitate faster progress, eg., in the development of lipid (and other) MD models. Naturally, such database would provide a fruitful platform to other machine learning applications as well.

## Acknowledgement

This material is based upon work supported by XXX under Grant No. XXX. The project is/isn't part of the NMRlipids open collaboration (nmrlipids.blogspot.com)

## References

- (1) Rossmann, M. G.; Blow, D. M. The detection of sub-units within the crystallographic asymmetric unit. *Acta Crystallographica* **1962**, *15*, 24–31.
- (2) Burley, S. K.; Berman, H. M.; Christie, C.; Duarte, J. M.; Feng, Z.; Westbrook, J.; Young, J.; Zardecki, C. RCSB Protein Data Bank: Sustaining a living digital data resource that enables breakthroughs in scientific research and biomedical education. *Protein Science* **2018**, *27*, 316–330.
- (3) Kirchmair, J.; Markt, P.; Distinto, S.; Schuster, D.; Spitzer, G. M.; Liedl, K. R.; Langer, T.; Wolber, G. The Protein Data Bank (PDB), Its Related Services and Software Tools as Key Components for In Silico Guided Drug Discovery. *Journal of Medicinal Chemistry* **2008**, *51*, 7021–7040.
- (4) Huang, P.-S.; Boyken, S. E.; Baker, D. The coming of age of de novo protein design. *Nature* **2016**, *537*, 320.
- (5) Hobohm, U.; Scharf, M.; Schneider, R.; Sander, C. Selection of representative protein data sets. *Protein Science* **1992**, *1*, 409–417.
- (6) Levitt, M. Growth of novel protein structural data. *Proceedings of the National Academy of Sciences* **2007**, *104*, 3183–3188.
- (7) Mészáros, B.; Dosztányi, Z.; Fichó, E.; Magyar, C.; Simon, I. In *Computational Methods to Study the Structure and Dynamics of Biomolecules and Biomolecular Processes: From Bioinformatics to Molecular Quantum Mechanics*; Liwo, A., Ed.; Springer International Publishing: Cham, 2019; pp 561–596.
- (8) Sercombe, L.; Veerati, T.; Moheimani, F.; Wu, S. Y.; Sood, A. K.; Hua, S. Advances and Challenges of Liposome As-



- sisted Drug Delivery. *Frontiers in Pharmacology* **2015**, *6*, 286.
- (9) Chau, P.-L.; Hoang, P. N.; Picaud, S.; Jedlovsky, P. A possible mechanism for pressure reversal of general anaesthetics from molecular simulations. *Chemical Physics Letters* **2007**, *438*, 294 – 297.
  - (10) Ferreira, T. M.; Coreta-Gomes, F.; Ollila, O. H. S.; Moreno, M. J.; Vaz, W. L. C.; Topgaard, D. Cholesterol and POPC segmental order parameters in lipid membranes: solid state  $1\text{H}$ – $13\text{C}$  NMR and MD simulation studies. *Phys. Chem. Chem. Phys.* **2013**, *15*, 1976–1989.
  - (11) Lindahl, E.; Sansom, M. S. Membrane proteins: molecular dynamics simulations. *Current Opinion in Structural Biology* **2008**, *18*, 425 – 431, Membranes / Engineering and design.
  - (12) Lyubartsev, A. P.; Rabinovich, A. L. Recent development in computer simulations of lipid bilayers. *Soft Matter* **2011**, *7*, 25–39.
  - (13) Botan, A.; Favela-Rosales, F.; Fuchs, P. F. J.; Javanainen, M.; Kanduč, M.; Kulig, W.; Lamberg, A.; Loison, C.; Lyubartsev, A.; Miettinen, M. S. et al. Toward Atomistic Resolution Structure of Phosphatidylcholine Headgroup and Glycerol Backbone at Different Ambient Conditions. *The Journal of Physical Chemistry B* **2015**, *119*, 15075–15088, PMID: 26509669.
  - (14) Ferreira, T. M.; Ollila, O. H. S.; Pigliapochi, R.; Dabkowska, A. P.; Topgaard, D. Model-free estimation of the effective correlation time for C–H bond reorientation in amphiphilic bilayers:  $1\text{H}$ – $13\text{C}$  solid-state NMR and MD simulations. *The Journal of Chemical Physics* **2015**, *142*, 044905.
  - (15) Miettinen, M. S.; Lipowsky, R. Bilayer membranes with frequent flip-flops have tensionless leaflets. *Nano letters* **2019**, *?*, ?–?
  - (16) Vogel, A.; Feller, S. E. Headgroup Conformations of Phospholipids from Molecular Dynamics Simulation: Sampling Challenges and Comparison to Experiment. *The Journal of Membrane Biology* **2012**, *245*, 23–28.
  - (17) Chernomordik, L. V.; Kozlov, M. M. Mechanics of membrane fusion. *Nature structural & molecular biology* **2008**, *15*, 675.
  - (18) Gibson, N. J.; Brown, M. F. Lipid head-group and acyl chain composition modulate the MI-MII equilibrium of rhodopsin in recombinant membranes. *Biochemistry* **1993**, *32*, 2438–2454, PMID: 8443184.
  - (19) Phillips, R.; Ursell, T.; Wiggins, P.; Sens, P. Emerging roles for lipids in shaping membrane-protein function. *Nature* **2009**, *459*, 379.
  - (20) Feller, S. E.; Gawrisch, K.; MacKerell, A. D. Polyunsaturated Fatty Acids in Lipid Bilayers: Intrinsic and Environmental Contributions to Their Unique Physical Properties. *Journal of the American Chemical Society* **2002**, *124*, 318–326, PMID: 11782184.
  - (21) Eldho, N. V.; Feller, S. E.; Tristram-Nagle, S.; Polozov, I. V.; Gawrisch, K. Polyunsaturated Docosahexaenoic vs Docosapentaenoic Acid Differences in Lipid Matrix Properties from the Loss of One Double Bond. *Journal of the American Chemical Society* **2003**, *125*, 6409–6421, PMID: 12785780.
  - (22) Wohllert, J.; Edholm, O. Dynamics in atomistic simulations of phospholipid membranes: Nuclear magnetic resonance relaxation rates and lateral diffusion. *The Journal of Chemical Physics* **2006**, *125*, 204703.
  - (23) Klauda, J. B.; Roberts, M. F.; Redfield, A. G.; Brooks, B. R.; Pastor, R. W. Rotation of Lipids in Membranes: Molecular Dynamics Simulation,  $31\text{P}$  Spin-Lattice Relaxation, and Rigid-Body Dy-

- namics. *Biophysical Journal* **2008**, *94*, 3074–3083.
- (24) Leftin, A.; Brown, M. F. An NMR database for simulations of membrane dynamics. *Biochimica et Biophysica Acta (BBA) - Biomembranes* **2011**, *1808*, 818 – 839, Including the Special Section: Protein translocation across or insertion into membranes.
- (25) Klauda, J. B.; Eldho, N. V.; Gawrisch, K.; Brooks, B. R.; Pastor, R. W. Collective and Noncollective Models of NMR Relaxation in Lipid Vesicles and Multilayers. *The Journal of Physical Chemistry B* **2008**, *112*, 5924–5929, PMID: 18179193.
- (26) Catte, A.; Giryh, M.; Javanainen, M.; Loison, C.; Melcr, J.; Miettinen, M. S.; Monticelli, L.; Määttä, J.; Oganessian, V. S.; Ollila, O. H. S. et al. Molecular electrometer and binding of cations to phospholipid bilayers. *Phys. Chem. Chem. Phys.* **2016**, *18*, 32560–32569.
- (27) Ollila, S.; Hyvönen, M. T.; Vattulainen, I. Polyunsaturation in Lipid Membranes: Dynamic Properties and Lateral Pressure Profiles. *J. Phys. Chem. B* **2007**, *111*, 3139–3150.
- (28) Ollila, O. H. S.; Ferreira, T.; Topgaard, D. MD simulation trajectory and related files for POPC bilayer (Berger model delivered by Tieleman, Gromacs 4.5). 2014; {<http://dx.doi.org/10.5281/zenodo.13279>}.
- (29) Klauda, J. B.; Venable, R. M.; Freites, J. A.; O'Connor, J. W.; Tobias, D. J.; Mondragon-Ramirez, C.; Vorobyov, I.; Jr, A. D. M.; Pastor, R. W. Update of the CHARMM All-Atom Additive Force Field for Lipids: Validation on Six Lipid Types. *J. Phys. Chem. B* **2010**, *114*, 7830–7843.
- (30) Santuz, H. MD simulation trajectory and related files for POPC bilayer (CHARMM36, Gromacs 4.5). 2015; <http://dx.doi.org/10.5281/zenodo.14066>, DOI: 10.5281/zenodo.14066.
- (31) Antila, H. . 2018; <http://dx.doi.org/10.5281/zenodo.148560>, DOI: 10.5281/zenodo.1468560.
- (32) Kulig, W.; Jurkiewicz, P.; Olżyńska, A.; Tynkkynen, J.; Javanainen, M.; Manna, M.; Rog, T.; Hof, M.; Vattulainen, I.; Jungwirth, P. Experimental determination and computational interpretation of biophysical properties of lipid bilayers enriched by cholesterol hemisuccinate. *Biochim. Biophys. Acta* **2015**, *1848*, 422 – 432.
- (33) Javanainen, M. POPC/Cholesterol @ 310K. 0, 10, 40, 50 and 60 mol-cholesterol. Model by Maciejewski and Rog. **2015**,
- (34) Dickson, C. J.; Madej, B. D.; Skjevik, A. A.; Betz, R. M.; Teigen, K.; Gould, I. R.; Walker, R. C. Lipid14: The Amber Lipid Force Field. *J. Chem. Theory Comput.* **2014**, *10*, 865–879.
- (35) Ollila, O. H. S.; Retegan, M. MD simulation trajectory and related files for POPC bilayer (Lipid14, Gromacs 4.5). 2014; DOI: 10.5281/zenodo.12767.
- (36) Jämbeck, J. P. M.; Lyubartsev, A. P. An Extension and Further Validation of an All-Atomistic Force Field for Biological Membranes. *J. Chem. Theory Comput.* **2012**, *8*, 2938–2948.
- (37) Javanainen, M. POPC with 0, 10, 20, and 30 mol-Slipids force field. 2016; <http://dx.doi.org/10.5281/zenodo.3243328>.
- (38) Melcr, J.; Martinez-Seara, H.; Nencini, R.; Kolafa, J.; Jungwirth, P.; Ollila, O. H. S. Accurate Binding of Sodium and Calcium to a POPC Bilayer by Effective Inclusion of Electronic Polarization. *The Journal of Physical Chemistry B* **2018**, *122*, 4546–4557.
- (39) Melcr, J. Simulations of POPC lipid bilayer in water solution at various NaCl, KCl and CaCl<sub>2</sub> concentrations using ECC-POPC force field. **2019**,

- (40) Hltje, M.; Frster, T.; Brandt, B.; Engels, T.; von Rybinski, W.; Hltje, H.-D. Molecular dynamics simulations of stratum corneum lipid models: fatty acids and cholesterol. *Biochim. Biophys. Acta* **2001**, *1511*, 156 – 167.
- (41) Ollila, O. H. S. MD simulation trajectory and related files for POPC/cholesterol (50 molmodified Hltje, Gromacs 4.5). **2014**,
- (42) Lim, J. B.; Rogaski, B.; Klauda, J. B. Update of the Cholesterol Force Field Parameters in CHARMM. *J. Phys. Chem. B* **2012**, *116*, 203–210.
- (43) Santuz, H. MD simulation trajectory for POPC/50% Chol bilayer (CHARMM36, Gromacs 4.5). 2015; <http://dx.doi.org/10.5281/zenodo.14068>, DOI: 10.5281/zenodo.14068.
- (44) Jmbeck, J. P. M.; Lyubartsev, A. P. Another Piece of the Membrane Puzzle: Extending Slipids Further. *Journal of Chemical Theory and Computation* **2013**, *9*, 774–784, PMID: 26589070.
- (45) Kanduc, M.; Schneck, E.; Netz, R. R. Hydration Interaction between Phospholipid Membranes: Insight into Different Measurement Ensembles from Atomistic Molecular Dynamics Simulations. *Langmuir* **2013**, *29*, 9126–9137.
- (46) Kanduc, M. MD trajectory for DLPC bilayer (Berger, Gromacs 4.5.4), nw=24 w/l. 2015; DOI: 10.5281/zenodo.16289.
- (47) Kanduc, M. MD trajectory for DLPC bilayer (Berger, Gromacs 4.5.4), nw=16 w/l. 2015; DOI: 10.5281/zenodo.16292.
- (48) Kanduc, M. MD trajectory for DLPC bilayer (Berger, Gromacs 4.5.4), nw=12 w/l. 2015; DOI: 10.5281/zenodo.16293.
- (49) Ollila, O. H. S. MD simulation trajectory and related files for POPC bilayer in low hydration (Berger model delivered by Tieleman, Gromacs 4.5). **2015**,
- (50) Kanduc, M. MD trajectory for DLPC bilayer (Berger, Gromacs 4.5.4), nw=4 w/l. 2015; DOI: 10.5281/zenodo.16295.
- (51) Ollila, O. H. S.; Miettinen, M. MD simulation trajectory and related files for POPC bilayer in medium low hydration (CHARMM36, Gromacs 4.5). 2015; <http://dx.doi.org/10.5281/zenodo.13946>, DOI: 10.5281/zenodo.13946.
- (52) Ollila, O. H. S.; Miettinen, M. MD simulation trajectory and related files for POPC bilayer in low hydration (CHARMM36, Gromacs 4.5). 2015; <http://dx.doi.org/10.5281/zenodo.13945>, DOI: 10.5281/zenodo.13945.
- (53) Javanainen, M. POPC @ 310K, varying water-to-lipid ratio. Model by Maciejewski and Rog. 2014; <http://dx.doi.org/10.5281/zenodo.13498>, DOI: 10.5281/zenodo.13498.
- (54) Venable, R. M.; Luo, Y.; Gawrisch, K.; Roux, B.; Pastor, R. W. Simulations of Anionic Lipid Membranes: Development of Interaction-Specific Ion Parameters and Validation Using NMR Data. *J. Phys. Chem. B* **2013**, *117*, 10183–10192.
- (55) Ollila, O. H. S. MD simulation trajectory and related files for POPC bilayer with 350mM NaCl (CHARMM36, Gromacs 4.5). 2015; <http://dx.doi.org/10.5281/zenodo.32496>.
- (56) Ollila, O. H. S. MD simulation trajectory and related files for POPC bilayer with 690mM NaCl (CHARMM36, Gromacs 4.5). 2015; <http://dx.doi.org/10.5281/zenodo.32497>.
- (57) Ollila, O. H. S. MD simulation trajectory and related files for POPC bilayer with 950mM NaCl (CHARMM36, Gromacs 4.5). 2015; <http://dx.doi.org/10.5281/zenodo.32498>.
- (58) Åqvist, J. Ion-water interaction potentials derived from free energy perturbation sim-

- ulations. *J. Phys. Chem.* **1990**, *94*, 8021–8024.
- (59) Javanainen, M.; Tynkkynen, J. POPC @ 310K, varying amounts of NaCl. Model by Maciejewski and Rog. 2015; <http://dx.doi.org/10.5281/zenodo.14976>.
- (60) Smith, D. E.; Dang, L. X. Computer simulations of NaCl association in polarizable water. *J. Chem. Phys* **1994**, *100*, 3757–3766.
- (61) Javanainen, M. POPC @ 310K, 130 mM of NaCl. Slipids with ions by Smith & Dang. 2015; <http://dx.doi.org/10.5281/zenodo.35275>.
- (62) Javanainen, M. POPC with varying amounts of cholesterol, 1 M of NaCl. Slipids with ions by Smith & Dang. 2015; <http://dx.doi.org/10.5281/zenodo.259341>.
- (63) Schlenkrich, M.; Brickmann, J.; MacKerell, A. D.; Karplus, M. *Biological Membranes*; Springer, 1996; pp 31–81.
- (64) Feller, S. E.; MacKerell, A. D. An improved empirical potential energy function for molecular simulations of phospholipids. *The Journal of Physical Chemistry B* **2000**, *104*, 7510–7515.
- (65) Leeb, F.; Maibaum, L. Spatially Resolving the Condensing Effect of Cholesterol in Lipid Bilayers. *Biophysical Journal* **2018**, *115*, 2179 – 2188.
- (66) Pham, Q. D.; Topgaard, D.; Sparr, E. Cyclic and Linear Monoterpenes in Phospholipid Membranes: Phase Behavior, Bilayer Structure, and Molecular Dynamics. *Langmuir* **2015**, *31*, 11067–11077, PMID: 26375869.
- (67) Ulrich, A.; Watts, A. Molecular response of the lipid headgroup to bilayer hydration monitored by 2H-NMR. *Biophys. J.* **1994**, *66*, 1441 – 1449.
- (68) Bechinger, B.; Seelig, J. Conformational changes of the phosphatidylcholine head-group due to membrane dehydration. A 2H-NMR study. *Chemistry and Physics of Lipids* **1991**, *58*, 1 – 5.
- (69) Volke, F.; Pampel, A. Membrane Hydration and Structure on a Subnanometer Scale as Seen by High Resolution Solid State Nuclear Magnetic Resonance: POPC and POPC/C<sub>12</sub>E0<sub>4</sub> Model Membranes. *Biophys. J.* **1995**, *68*, 1960–1965.
- (70) Seelig, J.; MacDonald, P. M.; Scherer, P. G. Phospholipid head groups as sensors of electric charge in membranes. *Biochemistry* **1987**, *26*, 7535–7541, PMID: 3322401.

## Graphical TOC Entry

TOC here if needed